Physics of Fluids

Energy harvesting from passive oscillation of inverted foil

Cite as: Phys. Fluids **33**, 075111 (2021); https://doi.org/10.1063/5.0056567
Submitted: 11 May 2021 . Accepted: 28 June 2021 . Published Online: 15 July 2021

Md. Mahbub Alam, Li-Ming Chao (朝黎明), Shafiqur Rehman, Chunning Ji (及春宁), and Hanfeng Wang (王汉封)

Energy harvesting from passive oscillation of inverted foil

Cite as: Phys. Fluids **33**, 075111 (2021); doi: 10.1063/5.0056567
Submitted: 11 May 2021 · Accepted: 28 June 2021 ·
Published Online: 15 July 2021

Md. Mahbub Alam,[1,a)] Li-Ming Chao (朝黎明),[1] Shafiqur Rehman,[2] Chunning Ji (及春宁),[3] and Hanfeng Wang (王汉封)[4]

AFFILIATIONS

[1] Center for Turbulence Control, Harbin Institute of Technology, Shenzhen 518055, China
[2] Interdisciplinary Research Center for Renewable Energy and Power Systems (IRC-REPS), Research Institute, King Fahd University of Petroleum and Minerals, Dhahran 31261, Saudi Arabia
[3] State Key Laboratory of Hydraulic Engineering Simulation and Safety, Tianjin University, Tianjin 300072, China
[4] School of Civil Engineering, Central South University, Changsha, China

[a)] **Author to whom correspondence should be addressed:** alam@hit.edu.cn and alamm28@yahoo.com

ABSTRACT

A numerical study is carried out to investigate the energy harvesting from an inverted foil undergoing flow-induced pitching oscillation for reduced velocity $Ur = 1$–45 and damping ratio $\zeta = 0$–0.295. The benchmark results with undamped foil ($\zeta = 0$) indicate that the foil does not oscillate for $Ur \le 27$ but does oscillate with increasing amplitude for $27 < Ur < 34$ and with constant amplitude for $Ur \ge 34$. Lissajous diagrams of moment coefficient against the foil displacement are linked to the energy harvesting, showing how Ur and ζ affect the oscillating amplitude, reduced frequency, wake structures, and power exchange between the foil and the flow. The energy harvesting efficiency η up to 15.06% is achieved at $Ur = 37$ and $\zeta = 0.130$ with a reduced frequency $f^* = 0.151$ that is used by the cruising aquatic animals. The foil oscillation with negative power enhances the growth of vortices while that with positive power weakens the growth.

I. INTRODUCTION

Since the Netherlandish windmills first used several hundred years ago, there is a long history of windmills to extract energy from a flowing fluid. The wind is a potential renewable energy resource to supplement traditional fossil fuels. On the other hand, the effectiveness of wind turbines is highly limited by the site[1] as the wind turbine causes considerable noise[2] and suffers from the cut-in speed. Compared to the wind turbines, the flapping foil energy harvester or vibrating cylinder energy harvester in water is more effective for small-scale operation, having less environmental inconvenience and more continual predictable power output.[3–8] Energy conversation from water current is much suitable for the coastal countries.[9]

The motion of an energy harvesting flapping foil is categorized into three, including prescribed, semipassive, and passive oscillation, depending on the foil activation process.[8] The prescribed motion is defined as that the flapping foil undergoes the given forced oscillation. Power is required to generate the forced motion. Hence, the flapping foil extracts energy from the flow when the time-averaged driving power for the prescribed motion is negative. Kinsey and Dumas[10] numerically investigated the power generation capacity of an oscillating foil undergoing pitching and plunging sinusoidal motion. The pitching center was $1/3c$ away from the leading edge, where c is the chord length. They found that the flow conditions related to the optimal efficiency are dominated by the formation and evolution of the leading-edge vortex (LEV). Following the work of Kinsey and Dumas,[10] a considerable effort has made to investigate the energy generation of a prescribed flapping motion.[11,12] It is found that the optimum non-dimensional frequency of a prescribed foil is similar to that used by flying and swimming animals.[13–15] In particular, Zhu[12] reported that the input power to drive a prescribed pitching foil is close to zero during the optimal energy extraction, suggesting the feasibility of the energy harvesting from a passive flapping foil.

The second mode, semipassive mode, denotes that the foil undergoes a prescribed pitching oscillation and a flow-induced plunging motion, and vice versa. The power can thus be extracted from the flow-induced oscillation where the load is usually modeled by a viscous damper.[16] Similar to the results from a prescribed flapping foil, the LEV formation is showed to play an important role in harvesting energy.[17–22] To achieve a higher energy harvesting efficiency, researchers also investigated the effect of nonsinusoidal prescribed motion on energy generation. Young *et al.*[23] simulated a fully passive NACA0012 flapping foil using a two-dimensional Navier–Stokes solver at a chord-based Reynolds number $Re = 1100$. The foil was allowed to oscillate about the pitching center $0.5c$ away from the leading edge. They found that the energy extraction efficiency can be significantly improved by controlling the timing and location of the LEV and its interaction with the trailing edge. It further suggests that undesirable dynamic stall in rotary turbines may be very beneficial in flapping foil harvesters. Li *et al.*[24] examined the effects of pitching motion profile on the energy harvesting performance of a semiactive flapping foil using the immersed boundary method at $Re = 1000$. Cosine-like pitching profile was found to be better than sine-like pitching profile for energy extracting efficiency.

In the passive mode, the motion of the foil is fully governed by the fluid–structure interaction. In such a case, the flow passing over the foil causes the foil oscillation that in turn modifies the flow. A fluid–structure coupling thus takes place. The energy harvesting from a passive flapping foil is significantly influenced by the foil geometry, spring stiffness, and flow conditions.[23,25–29] In general, the fluid–structure interaction may result in periodic flapping motion, irregular flapping motion, and rotating motion.[25] Interestingly, the promising efficiency reported by a prescribed flapping foil can be replicated with a passive flapping motion.[23] Hence, the energy harvesting from a passive flapping motion is reasonable to consider as one of the most effective technologies for the engineering application because the passive flapping harvester is more feasible than the others.

Recently, the fluid dynamics of an inverted foil undergoing self-induced flapping has been studied to understand the flight dynamics and locomotion of flying animals.[30–32] Here, the inverted foil is the foil with the clamped trailing edge and free leading edge.[33–36] Inspired by self-sustained large-amplitude motion employed by the insects, researchers studied the energy harvesting from an inverted piezoelectric flag since the inverted flag is supposed to have superior capabilities of harvesting energy from wind and water.[37–39] On the other hand, the dependence of power extraction on the foil geometry, spring stiffness, and damping load has been studied in the literature for a foil having a round leading edge and a sharp trailing edge. No investigation has been conducted on an inverted foil where the leading edge is sharp and the trailing edge is round. Naturally, a few questions pop up. What are the power and efficiency of an inverted foil? How is the free-oscillation amplitude dependent on reduced velocity? What is the interaction between the vortices generated from the leading and trailing edges? How do the vortices contribute to the work done on the foil? What are the optimum efficiency and corresponding load? What is the detailed physics of energy harvesting? This work aims to address the issues raised above and investigate the energy harvesting from a passive flapping foil to reveal the corresponding fluid–structure coupling mechanisms. The foil is set in the flow such that the sharp edge heads the semicircular edge and the foil is allowed to oscillate about the center of the semicircular edge. The flow reduced velocity is varied from $Ur = 1$ to 45.

II. COMPUTATIONAL APPROACH

A. Problem formulations

A schematic of the flow and model configuration is presented in Fig. 1(a). A two-dimensional foil of a chord length c is placed in a uniform flow of velocity U_∞ in the x-direction. The foil has a tapered leading edge and a semicircular trailing edge of thickness D [diameter of the semicircle, see Fig. 1(b)]. The dimensionless thickness, D/c, is 0.167. The rotation center of the foil is at point O that is the center of the semicircle and the origin of the Cartesian coordinate system.

Under a constant thickness-based Reynolds number $Re_D = U_\infty D/\nu = 150$, the foil is passively oscillated, where ν is the kinematic viscosity of the fluid. The governing equation of foil oscillation can be written as

$$I\ddot{\theta}(t) + c_\theta\dot{\theta}(t) + k_\theta\theta(t) = M(t), \tag{1}$$

where I is the moment of inertia of foil, c_θ denotes the torsional damping coefficient, k_θ represents the torsional spring stiffness, $\theta(t)$ is the time-dependent angular displacement [Fig. 1(b)], and $M(t)$ is the moment on the foil.

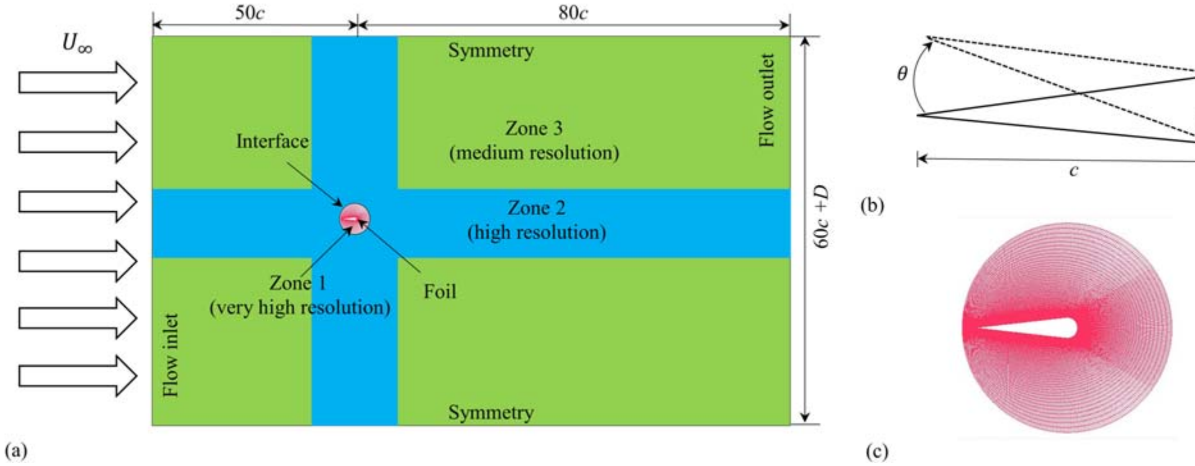

FIG. 1. (a) Computational domain and mesh system. (b) Foil and definitions of symbols. (c) Zoomed-in view of mesh around the foil.

Three dimensionless parameters are employed to characterize the flow-induced oscillation: the reduced velocity Ur, damping ratio ζ, and reduced frequency f^*, which are defined as

$$Ur = U_\infty / f_n D, \tag{2}$$

$$\zeta = c_\theta / 2\sqrt{I k_\theta}, \tag{3}$$

and

$$f^* = fD/U_\infty, \tag{4}$$

where f_n and f are the natural frequency and passively oscillating frequency of the foil, respectively. The Ur is varied from 1 to 45 by changing f_n of the system.

Based on Eq. (1), the instantaneous moment coefficient of the foil is defined as

$$C_M(t) = \frac{M(t)}{0.5\rho U_\infty^2 c^2}, \tag{5}$$

where ρ is the fluid density. The instantaneous energy extracted from the flow by the oscillating foil is considered as

$$P(t) = M(t)\dot{\theta}(t). \tag{6}$$

Given the model is 2D, the instantaneous power coefficient is defined as

$$C_p(t) = \frac{P(t)}{0.5\rho U_\infty^3 c}. \tag{7}$$

The energy harvesting efficiency η is defined as the ratio of the power extracted from flow by the pitching foil and the total available energy in the oncoming flow passing through the swept area,

$$\eta = \frac{1}{nT}\frac{\displaystyle\int_t^{t+nT} M(t)\dot{\theta}(t)\mathrm{d}t}{0.5\rho U_\infty^3 c}, \tag{8}$$

where $T\,(= 1/f)$ is the oscillating period.

B. Numerical aspects

1. Numerical method

The unsteady flow field around a passively oscillating foil is simulated using the commercially available CFD package Fluent 15.0. For a Newtonian fluid, the governing equations describing the unsteady incompressible flow are the mass and momentum conservations,

$$\nabla \cdot \mathbf{u} = \mathbf{0} \tag{9}$$

and

$$\frac{\mathrm{D}\mathbf{u}}{\mathrm{D}t} + (\mathbf{u}\cdot\nabla)\mathbf{u} = -\frac{1}{\rho}\nabla p + \nu\nabla^2\mathbf{u}, \tag{10}$$

where $\mathbf{u}$ denotes the velocity vector and p is the static pressure.

The finite-volume method is used to achieve the spatial discretization of the Navier–Stokes equations [Eqs. (9) and (10)]. The second-order upwind scheme is used to discretize the spatial term, and the first-order implicit scheme is used to discretize the temporal term. The SIMPLEC algorithm is used to achieve the pressure-velocity coupling of the continuity equation [Eq. (9)]. Moreover, the Gauss–Seidel linear equation solver is employed to solve the discretized equations.

In this study, the computational domain is rectangular [Fig. 1(a)]. The inlet velocity boundary is at a distance of 50c from the oscillating center of the foil, with $\mathbf{u} = (U_\infty, 0)$. The $\partial\mathbf{u}/\partial\boldsymbol{x} = (0, 0)$ and $\partial p/\partial x = 0$ are used as the no-stress outflow boundary conditions. The outlet boundary is at a distance of 80c from the foil rotation center. The symmetry condition is used for the upper and lower boundaries located at a distance of 30c +D/2 from the central line of the foil.[40]

The computational domain is divided into three zones (zones 1, 2, and 3) of very high, high, and medium resolutions, respectively [Fig. 1(a)]. The very high resolution in grids is provided around the foil (zone 1) while the high resolution is given on the two sides of the wake centerline (zone 2) where the velocity gradient is large. Zone 3, away from the wake, has the medium resolution. The circular zone has a radius of 1.15c [Fig. 1(c)] where a circular nonconformal sliding grid interface is used.[40,41] The grids inside the circle move with the foil as a rigid body. An *O-xy* mesh system is employed in this circular zone, with the first cell at a distance of $10^{-2}D$ from the foil surface [Fig. 1(c)]. Beyond the circular zone, structured meshes are given. The grids close to the foil have a very high resolution to precisely resolve the boundary layer on the foil. The passive oscillation of the foil is handled by making the source term equal to the angular acceleration of the foil. The source term is added in the governing equations using a user defined function (UDF).

2. Grid- and time-independence tests

Before conducting extensive simulations, the mesh and time-step independence tests were performed. At time step $\Delta t = 4\times10^{-4}$ s, the grid-independence test is done for several sets of grids with 1.09×10^5 (M1), 1.23×10^5 (M2), and 1.5×10^5 (M3), corresponding to the 241, 261, and 321 points on the surface of the foil, respectively. The mesh refinement is performed at zones 1 and 2 [Fig. 1(a)]. Although the increase in the total number of grids with M1 = 1.09×10^5, M2 = 1.23×10^5, and M3 = 1.5×10^5 is about 13% (between M1 and M2) and 22% (between M2 and M3), respectively, the grid resolution in zone 1 increases by 47% (between M1 and M2) and 96% (between M2 and M3), given that no grid refinement is made in zone 3. The increase in the grid number in zone 2 is about 25% in either step.

The time histories of moment coefficient over one cycle for the three grid systems are presented in Fig. 2(a), while its root mean square values ($C_M^{'}$) are provided in Table I. The mesh M2 from Table I is chosen for the time-independence test.

With M2, four time steps $\Delta t = 4\times10^{-4}$, 2×10^{-4}, 1×10^{-4}, and 0.8×10^{-4} s are adopted. The corresponding C'_M values and time histories are presented in Table II and Fig. 2(b), respectively. The difference in the results between $\Delta t2$ and $\Delta t4$ is 0.86% only. Considering the accuracy and computational resources, the $\Delta t = 2\times10^{-4}$ is chosen for the present work.

3. Validations

Following Robertson *et al.*[42] who investigated rotational galloping of a rectangular cylinder with aspect ratio 4, we choose the rectangular cylinder model (aspect ratio 4) to validate rotational galloping response at a Reynolds number of 250. Figure 2(c) presents a comparison of the rotational displacement $\theta(t)$ histories from the present and the simulations of Robertson *et al.* A good agreement is achieved between the present and the results of Robertson *et al.*, the maximum deviation in amplitudes between the two responses being less than 3%.

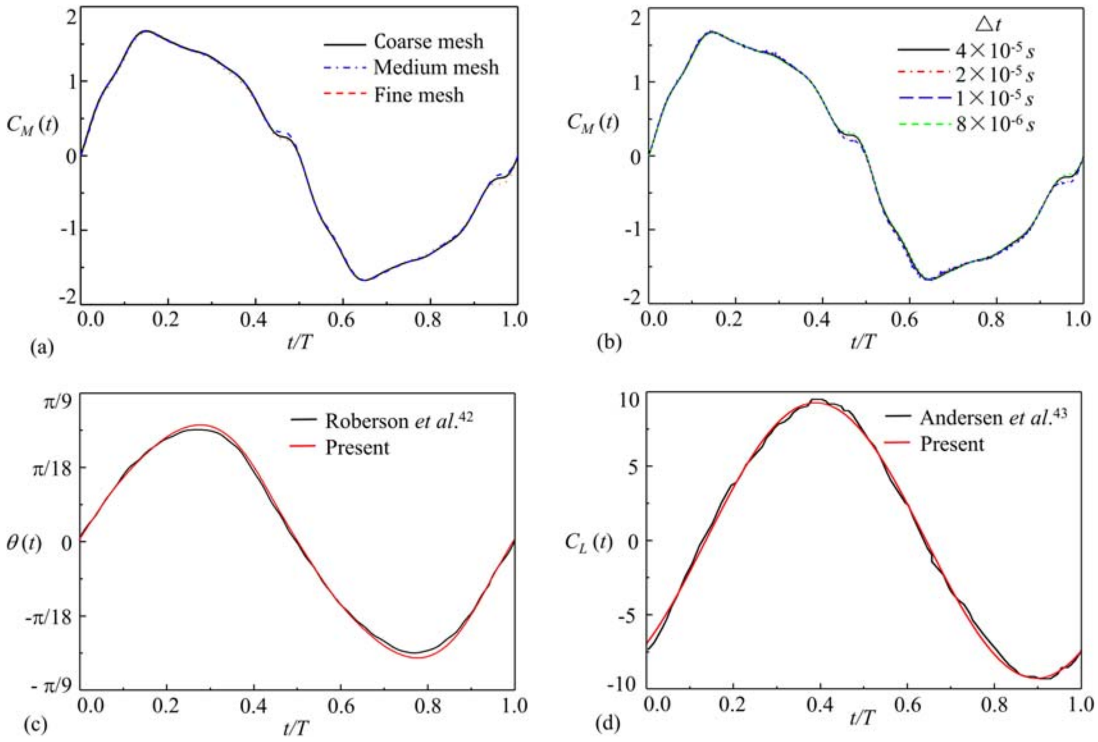

FIG. 2. Numerical validations. (a) Grid dependence tests. (b) Time-step dependence tests. (c) Comparison between present and the results of Roberson *et al.*[42] for a rectangular cylinder with cross-sectional aspect ratio 4, $Re = 250$, $Ur = 40$, and $\zeta = 0.25$. (d) Comparison of instantaneous lift coefficient $C_L(t)$ between present work and the work by Andersen *et al.*[43] work for a pitching foil at $St_D = 0.22$, $A_D = 1.81$, and $Re_D = 440$.

TABLE I. Grid-independence test results with $\Delta t = 4 \times 10^{-4}$ s.

Mesh	M1	M2	M3
Grid numbers	1.09×10^5	1.23×10^5	1.5×10^5
C'_M	1.142	1.149	1.154
Difference of C'_M	1.0%	0.43%	…

To further validate our numerical approach, we simulated a pitching foil at the thickness-based Reynolds number $Re_D = 440$ to compare our results with the experimental and numerical results of Andersen *et al.*[43] They conducted experiments in a soap film tunnel and simulations in a two-dimensional domain. The foil model in the work of Andersen *et al.* and our work is the same. We, therefore, considered the work of Andersen *et al.* as the benchmark to validate our work. The foil with the tapered trailing edge was given forced pitching at a thickness-based Strouhal number $St_D = D/U_\infty T = 0.22$, and a dimensionless pitching amplitude $A_D = A/D = 1.81$, where A is the peak-to-peak pitching amplitude. A comparison of $C_L(t)$ between the present and the work of Andersen *et al.* is made in Fig. 2(d). A good agreement in $C_L(t)$ is achieved between the present and the results of Andersen *et al.*

TABLE II. Time-independence test results with M2.

Time-step	$\Delta t1$	$\Delta t2$	$\Delta t3$	$\Delta t4$
Time-step (s)	4×10^{-4}	2×10^{-4}	1×10^{-4}	0.8×10^{-4}
C'_M	1.149	1.159	1.166	1.169
Difference of C'_M	1.71%	0.86%	0.26%	…

III. RESULTS AND DISCUSSION

The energy harvesting from a passively oscillating foil undergoing the flow-induced motion is systematically investigated with changing reduced velocity $Ur = 1$–45 with $\Delta Ur = 1$ and damping ratios $\zeta = 0$–0.295. The results for the $\zeta = 0$ case are presented first, followed by the results for ζ and Ur impacts on the energy extraction.

A. Undamped foil oscillation

The dependence of the foil response on Ur with $\zeta = 0$ as the baseline is shown in Fig. 3(a), where the maximum amplitude θ_0 is measured. There are three scenarios of the passive oscillation of the foil, including stationary ($\theta_0 = 0$) for $Ur \leq 27$, increasing θ_0 for $27 < Ur < 34$, and almost constant amplitude vibration ($\theta_0 \approx 0.54\pi$) for $Ur \geq 34$. In other words, θ_0 rapidly increases from 0 to 0.54π in a small range of Ur ($27 < Ur < 34$) before reaching a constant $\theta_0 \approx 0.54\pi$ (red dash line) that is slightly more than $\pi/2$. One can now easily understand why θ_0 lies slightly beyond 0.5π. It is due to fact that the foil during its oscillation has the longest bluff width (foil chord-length projection normal to the flow) at $\theta_0 = 0.5\pi$ after which the bluff width shrinks and the flow-induced moment reduces.

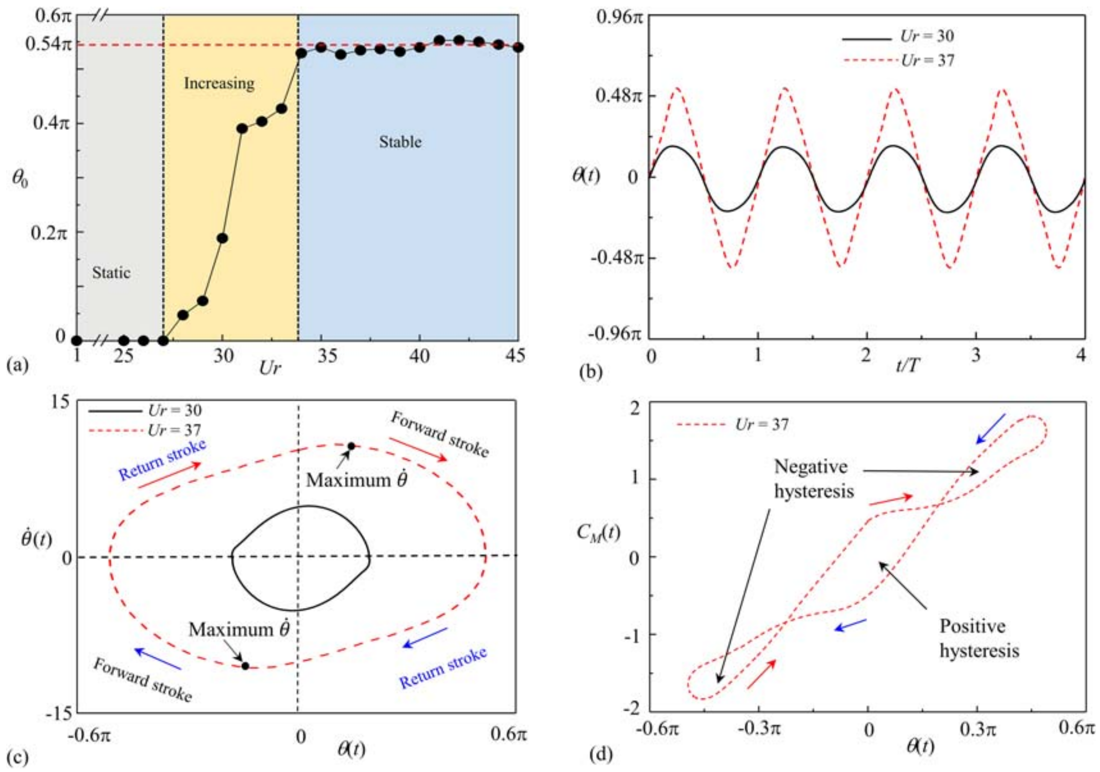

FIG. 3. (a) Dependence of θ_0 on *Ur*. (b) Time histories of $\theta(t)$. (c) Phase planes of $\dot{\theta}(t)$ vs $\theta(t)$. (d) Phase plane of $C_M(t)$ vs $\theta(t)$ at $Ur = 37$ with $\zeta = 0$. The red and blue arrows denote the upstroke and downstroke, respectively.

The time histories of θ for two representative $Ur = 30$ and 37 are illustrated in Fig. 3(b). At $Ur = 30$, it is seen that the time required from $\theta = 0$ to θ_0 [forward stroke (FS)] is smaller than that from $\theta = \theta_0$ to 0 (return stroke). That is, the foil travels faster in the forward stroke than in the return stroke. In the present work, the forward and return strokes are defined as the foil pitches from the zero position to the upper or lower extreme and from the upper or lower extreme to zero position, respectively. The Lissajous diagrams for $Ur = 30$ and 37 are presented in Fig. 3(c) to show the oscillation characteristics. It is seen that the passive oscillation of the foil with the sharp-edge upstream does not follow the standard sine trajectory, i.e., elliptical Lissajous curve. For a standard sine curve appearing for a free oscillation of a foil with the sharp-edge downstream, the magnitude of $\dot{\theta}$ will be maximum and minimum at $\theta = 0$ and θ_0, respectively. As illustrated in Fig. 3(c), $\dot{\theta}$ value is not maximum at $\theta = 0$ but is slightly away from $\theta = 0$, e.g., $\dot{\theta}$ magnitude is maximum at $|\theta| = 0.12\pi$ for $Ur = 37$ as marked in Fig. 3(c). That is, the foil experiences the acceleration–deceleration locomotion in the forward stroke. The acceleration arises from the fact that when the foil travels from $\theta = 0$, it gains effective bluffness and C_M becoming positive grows [Fig. 3(d)]. Comparing $\dot{\theta}$ values in the forward and return strokes, it is understood that $\dot{\theta}$ at a given θ is larger in the forward stroke ($\theta = 0 \rightarrow \theta_0$) than in the return stroke ($\theta = \theta_0 \rightarrow 0$). It suggests that the return stroke requires a longer time than the forward strokes.

Figure 3(d) illustrates the phase plane of C_M vs θ (in radian) at $Ur = 37$. The positive hysteresis describes that the phase difference between C_M and θ is positive while the negative hysteresis demonstrates the phase of θ advances that of C_M. Thus, the positive hysteresis indicates that the foil oscillation is driven by the flow. That is, the foil harvests energy from the fluid. On the other hand, in the negative hysteresis, the foil transfers the energy into the fluid. The positive hysteresis takes place when the foil is around $\theta = 0$, i.e., $|\theta| < \theta_0/2$, while the negative hysteresis persists at $|\theta| > \theta_0/2$. As seen in Fig. 3(d), the total size of the positive hysteresis region is the same as that of the negative hysteresis region, given $\zeta = 0$. The foil thus extracts no net power in one oscillation cycle. To further explore instantaneous power, the time histories of θ (blue line), $\dot{\theta}$ (green line), C_M (black line), and power coefficient C_p (red line) are presented in Fig. 4 at $Ur = 37$, $\zeta = 0$. Four phases are identified and classified over one oscillation cycle, where phase I is defined as 0.00–0.21T and 0.96–1.00T, phase II is defined as 0.21–0.46T, phase III is defined as 0.46–0.71T, and phase IV is defined as 0.74–0.96T. Positive C_p emerges at phases I and III while negative C_p appears in phases II and IV. Interestingly, the forward and return strokes mostly correspond to positive and negative C_p, respectively, which makes the net power in one oscillation cycle zero. More discussions about the phase classification and its physical significance will be made later for $\zeta \neq 0$.

B. Damped foil oscillation

1. *Flow-induced response and moment*

Based on the results for $\zeta = 0$, it is understood that the foil undergoes the self-sustained large-amplitude oscillation when $Ur \geq 34$ [Fig. 3(a)] that is auspicious for stable energy harvesting. Here, the

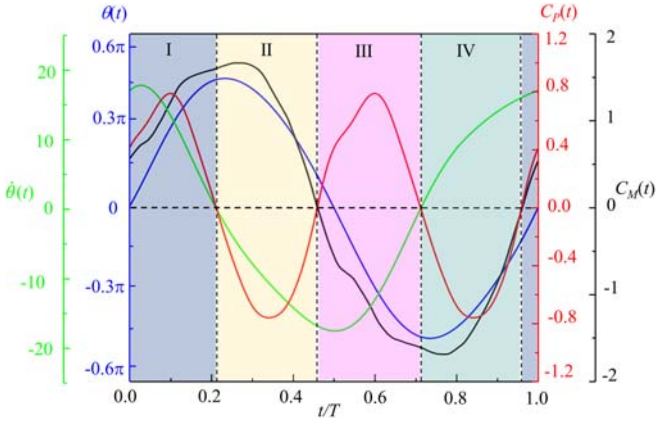

FIG. 4. Time histories of $\dot{\theta}(t)$ (green line), $\theta(t)$ (blue line), C_p(t) (red line), and C_M(t) (black line) at $Ur = 37$ and no damping ($\zeta = 0$).

loading (damping) effects on energy extraction is provided at a representative $Ur = 37$, where a series of damping ratios is considered, i.e., $\zeta = 0.035$, 0.055, 0.085, 0.115, 0.130, 0.175, 0.235, and 0.295.

Figure 5 illustrates the phase planes of C_M vs θ which demonstrates the effects of ζ on the energy generation in one oscillation cycle at $Ur = 37$. Two scenarios of hysteresis, including positive and negative hysteresis, are employed to describe the energy exchange between the foil and fluid over the upstroke and downstroke. When the foil undergoes the positive hysteresis, the foil harvests energy from the fluid which can be considered as the net positive power exchange. On the other hand, the negative hysteresis demonstrates the negative power exchange, i.e., energy transferring from the foil to the fluid. Hence, the difference in sizes between the positive and negative hysteresis regions essentially represents the amount of net energy extraction. At a small $\zeta < 0.115$, two negative small hysteresis regions are observed at large $|\theta|$ while one positive hysteresis region occurs at small $|\theta|$, around the equilibrium position. With increasing ζ from 0.035, the negative hysteresis regions shrink and vanish at $\zeta = 0.130$ while the positive hysteresis region enlarges. For $\zeta > 0.130$, only the positive hysteresis region remains, i.e., the foil can harvest energy from the fluid over the whole oscillation cycle. The net positive hysteresis around the region shrinks with increasing $\zeta > 0.130$, with the growing hysteresis at large $|\theta|$ and weakened hysteresis at small $|\theta|$ (i.e., around $\theta = 0$). Overall, the positive hysteresis region is largest at $\zeta = 0.130$ that complements the maximum power extraction.

Figure 6 presents Lissajous diagrams for different ζ values, displaying how ζ affects the foil oscillation. Both θ_0 and $\dot{\theta}$ decrease with increasing in ζ from 0.035 to 0.295 as ζ physically reduces the oscillation amplitude. For $\zeta \leq 0.130$, the $\dot{\theta}$ magnitude first increases and then decreases in the forward strokes ($\theta = 0 \rightarrow \theta_0$), while monotonically increasing in the return strokes. That is, the maximum $\dot{\theta}$ magnitude

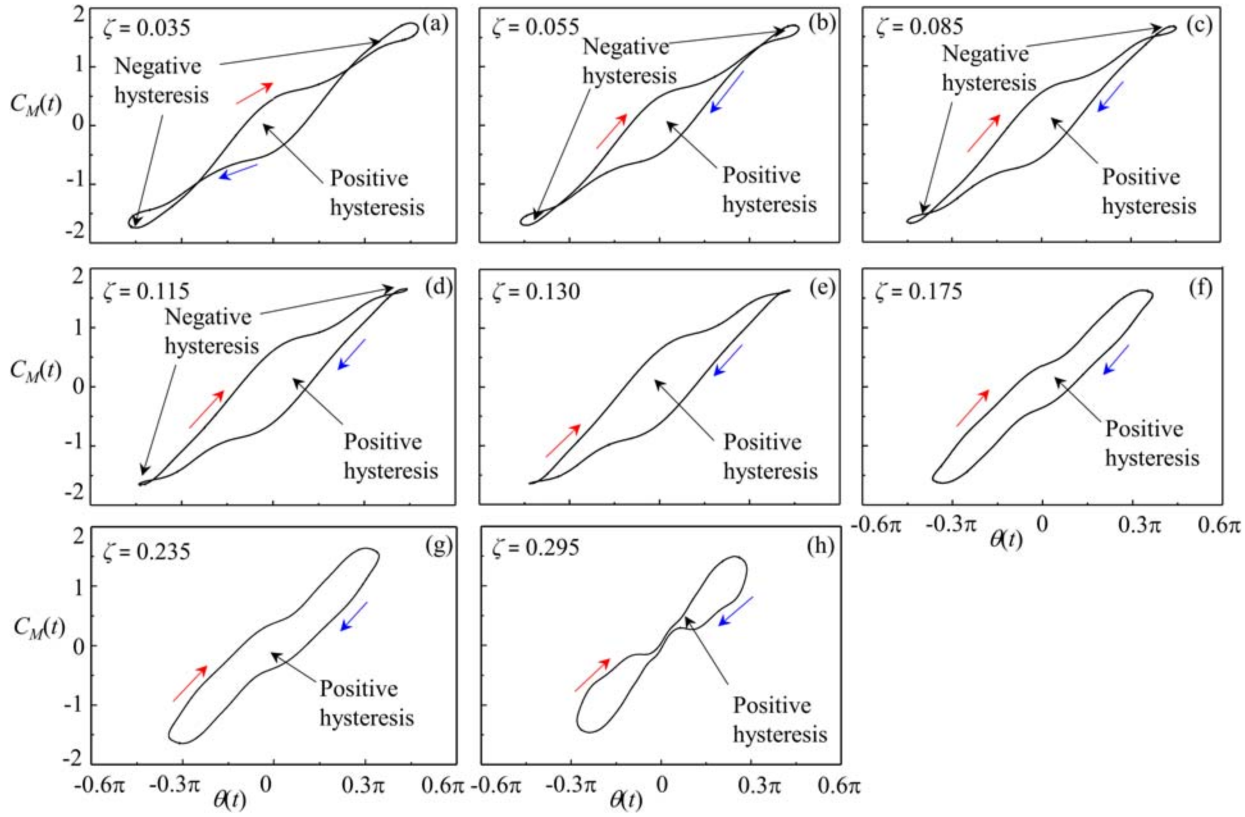

FIG. 5. Phase planes of $C_M(t)$ vs $\theta(t)$ at $Ur = 37$. (a) $\zeta = 0.035$, (b) $\zeta = 0.055$, (c) $\zeta = 0.085$, (d) $\zeta = 0.115$, (e) $\zeta = 0.130$, (f) $\zeta = 0.175$, (g) $\zeta = 0.235$, and (h) $\zeta = 0.295$.

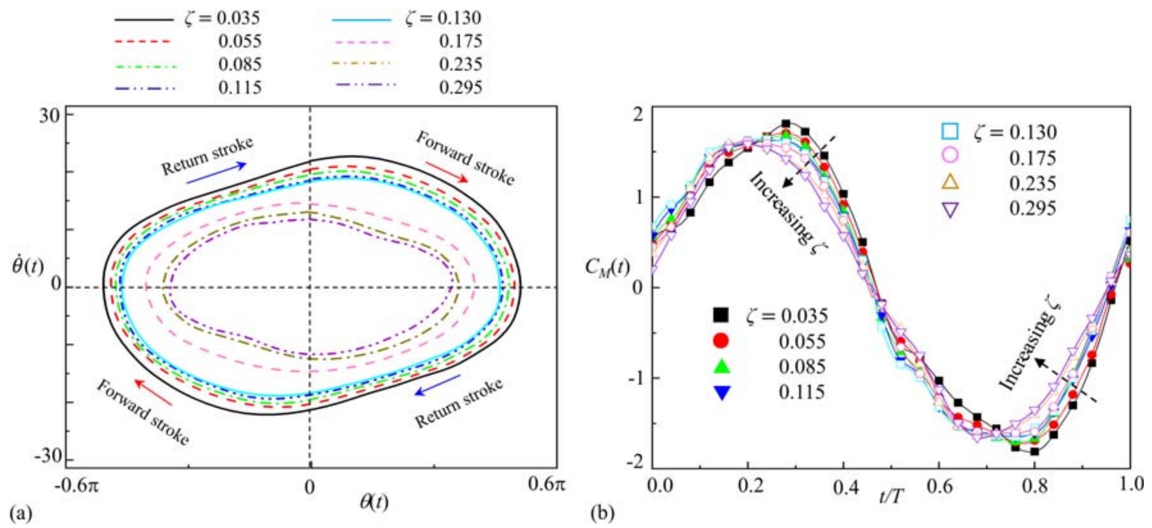

FIG. 6. (a) Lissajous diagrams of $\dot{\theta}(t)$ vs $\theta(t)$ and (b) time histories of $C_M(t)$ for different ζ values. $Ur = 37$.

occurs in the forward strokes after crossing $\theta = 0$. A comparison of $\dot{\theta}$ magnitudes in the forward and return strokes reflect that $\dot{\theta}$ at a given θ is larger in the forward stroke than in the return stroke. In other words, the forward stroke is faster than the return stroke. The scenario is opposite for $\zeta > 0.130$ where the maximum $\dot{\theta}$ magnitude prevails in the return strokes just before reaching $\theta = 0$, and $\dot{\theta}$ is smaller in the forward stroke than in the return stroke, i.e., now the return stroke is faster than the forward stroke. The $\zeta = 0.130$ can be considered as the boundary of the two scenarios, which conforms with the maximum net power generation observed in Fig. 5. Figure 6(b) displays that, with increasing ζ, the C_M peak declines and the occurrence of C_M peak advances. The negative hysteresis region appearing around $\theta = \theta_0$ thus gradually shrinks and disappears at $\zeta \geq 0.130$ (Fig. 5). In the return strokes (e.g., $0.25 \leq t/T \leq 0.50$ and $0.75 < t/T < 1.0$), C_M magnitude monotonically diminishes when ζ is increased. Interestingly, in most part of the forward stroke ($0 < t/T < 0.25$ and $0.45 < t/T < 0.65$), C_M magnitude increases with ζ increasing from 0.035 to 0.130 and then declines with further increasing ζ, maximum C_M magnitude occurring at $\zeta = 0.130$. As power is the product of C_M and $\dot{\theta}$, one can easily understand that the positive work done takes place mostly in the forward strokes (C_M and $\dot{\theta}$ both have the same sign) and negative work done prevails mostly in the return strokes (C_M and $\dot{\theta}$ having opposite signs). The large magnitude of C_M in the forward stroke for $\zeta = 0.130$, therefore, contributes to the power to be maximum at $\zeta = 0.130$ (Fig. 5).

2. Work done and efficiency

Figures 5 and 6 also reveal that θ_0 becomes small when ζ is increased. One may arise a question of how the foil oscillation frequency f^* changes when ζ is increased. It is thus worth investigating the dependence of θ_0 and f^* on ζ [Fig. 7(a)]. Being maximum at $\zeta = 0$, both θ_0 and f^* decrease with ζ. Damping provides a moment in the opposite direction of the rotation, the moment being proportional to

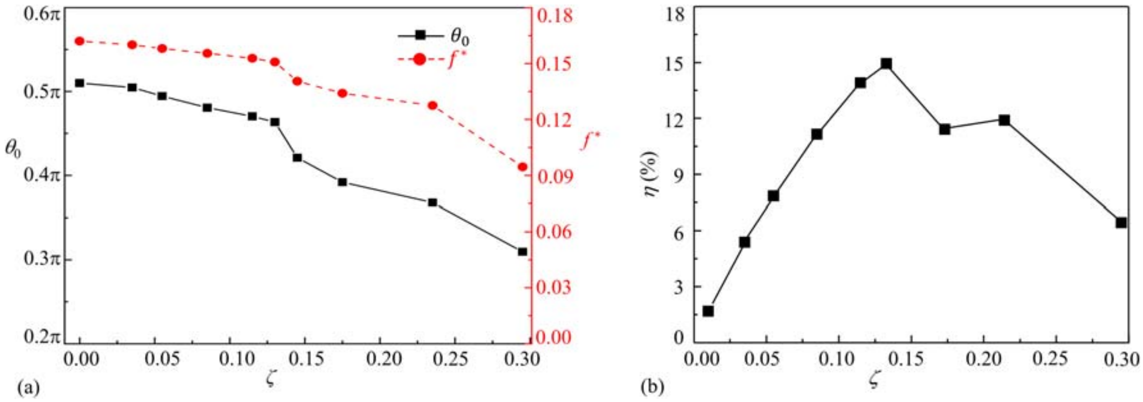

FIG. 7. Dependence of (a) θ_0 and f^* and (b) η on ζ at $Ur = 37$.

the angular velocity [Eq. (1)]. An increase in damping thus reduces the maximum amplitude and foil oscillation frequency. The decrease is however greater for $\zeta > 0.130$ than for $\zeta < 0.130$. Figure 7(b) shows the relationship of energy harvesting efficiency η with ζ. Interestingly, η grows from $\zeta = 0$ to 0.130 before declining for $\zeta > 0.130$. The maximum η of 15.06% is thus obtained at $\zeta = 0.130$, corresponding to the reduced frequency $f^* = 0.151$ that is generally adopted by the cruising aquatic animals[13–15] and is reported in a work on the energy harvesting from a prescribed foil by Young *et al.*[8] There is another small peak of η at $\zeta = 0.235$, but it does not represent the global peak. It perhaps arises from the nonlinear effect of ζ on C_M, $\dot{\theta}$ and phase lag between them.

To understand the energy harvesting mechanism, time histories of θ (blue line), $\dot{\theta}$ (green line), C_M (black line), and power coefficient C_p (red line) are presented in Fig. 8(a) for $Ur = 37$ and $\zeta = 0.130$. As the energy harvesting directly depends on the phase lag between $\dot{\theta}$ and C_M, four phases are identified and classified over one oscillation cycle. Moreover, we used the upstroke and downstroke to describe the foil pitching motion from the lower extreme to the upper extreme and from the upper extreme to the lower extreme, respectively.[44–46] Phase I is defined as 0–0.23T and 0.96T–T [D → A in Figs. 8(a) and 8(b)], located mostly in the forward stroke of the upstroke. Phases II and III lie mostly in the downstroke, following A → B (0.23–0.46T) and B → C (0.46–0.73T), respectively [Figs. 8(a) and 8(b)]. The rest of the region is phase IV denoted as C → D ($0.73 \le t \le 0.96T$) mostly lying in the return stroke of the upstroke [in Figs. 8(a) and 8(b)]. The foil captures energy from the fluid when $\dot{\theta}$ and C_M are of the same sign; on the other hand, it transmits energy to the fluid flow when $\dot{\theta}$ and C_M are of the opposite signs [Eq. (6)]. As illustrated in Fig. 8(a), $\dot{\theta} > 0$ and $C_M > 0$ in phase I, $\dot{\theta} < 0$ and $C_M > 0$ in phase II, $\dot{\theta} < 0$ and $C_M < 0$ in phase III, and $\dot{\theta} > 0$ and $C_M < 0$ in phase IV. Therefore, the foil extracts energy during phases I and III [+ symbol in Fig. 8(b)], while transferring energy to the fluid during phases II and IV [− symbol in Fig. 8(b)]. As the size of phases I and III is larger than that of phases II and IV, the foil harvests a net power over one cycle. In addition, the absolute value of the peak C_p in phases I and III is larger than that of the minimum C_p in phases II and IV, which also explains the foil harvesting net power from the fluid flow.

The effect of Ur on the energy harvesting is considered at $\zeta = 0.130$ with $Ur = 37$, 39, 42, and 45. The phase planes of C_M vs θ are presented in Fig. 9 that shows that the enveloped hysteresis region changes with increasing Ur. The hysteresis region narrows near $\theta \approx 0$ but swells around $\theta \approx \theta_0/2$. The former hinders the foil's capacity for energy extraction.

3. Connection between work done and flow structures

It is worth investigating the connection between vortex formation and energy extraction. As such, the vorticity structures and pressure distributions for $Ur = 37$ with $\zeta = 0.130$ are illustrated in Fig. 10 to explicate the connection between vortex formation, angular displacement, and energy extraction. The presented snapshots of spanwise vorticity ω^* ($= \omega D/U_\infty$) and pressure p^* distributions are for $\theta = \theta_0/2$ [Fig. 10(b), forward stroke], $\theta = \theta_0$ [Fig. 10(c), maximum displacement], $\theta = \theta_0/2$ [Fig. 10(d), retract stroke], and $\theta = 0$ [Fig. 10(e), mean position]. When the foil moves upward from point D that is slightly below the mean position, the work done is positive which could be understood from the fact that the lower surface undergoes higher pressure than the upper surface [Fig. 10(b2)]. The torque is thus positive, as is $\dot{\theta}$, and hence power. The upper boundary layer is mostly attached to the upper surface of the foil while the lower one separates from the foil tip and rolls weakly near the base, forming vortex P_1. With the foil moving from $\theta = \theta_0/2$ to $\theta = \theta_0$, the pressure on the front and rear surfaces increase and decrease, respectively [Fig. 10(c2)], consistent with the increasing $C_M(t)$ [Fig. 8(a)]. A strongly rolling clockwise vortex N_1 is generated from the foil tip, reducing the pressure behind the tip [Fig. 10(c1)]. As the foil returns from $\theta = \theta_0$ to $\theta = \theta_0/2$, both tip and base vortices (N_1 and P_1) strongly roll, and the highly negative pressure region behind the foil shifts from the tip to the base [Fig. 10(d)]. The lower surface still experiences a higher pressure than the upper surface; that is, the C_M

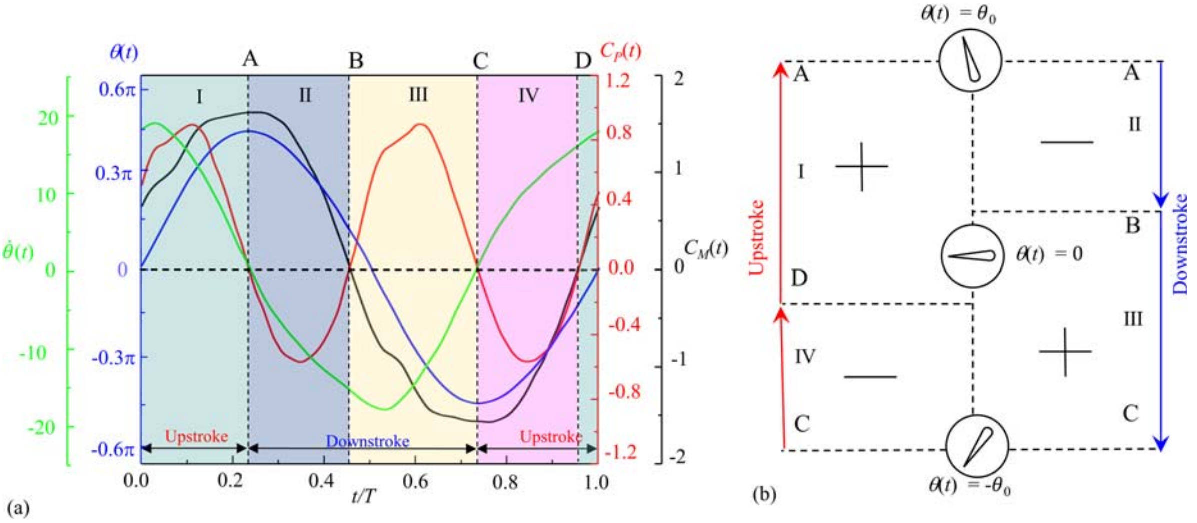

FIG. 8. (a) Time histories of $\dot{\theta}(t)$ (green line), $\theta(t)$ (blue line), $C_p(t)$ (red line), and $C_M(t)$ (black line) at $Ur = 37$ and $\zeta = 0.130$. (b) Power exchange diagram in one oscillation cycle.

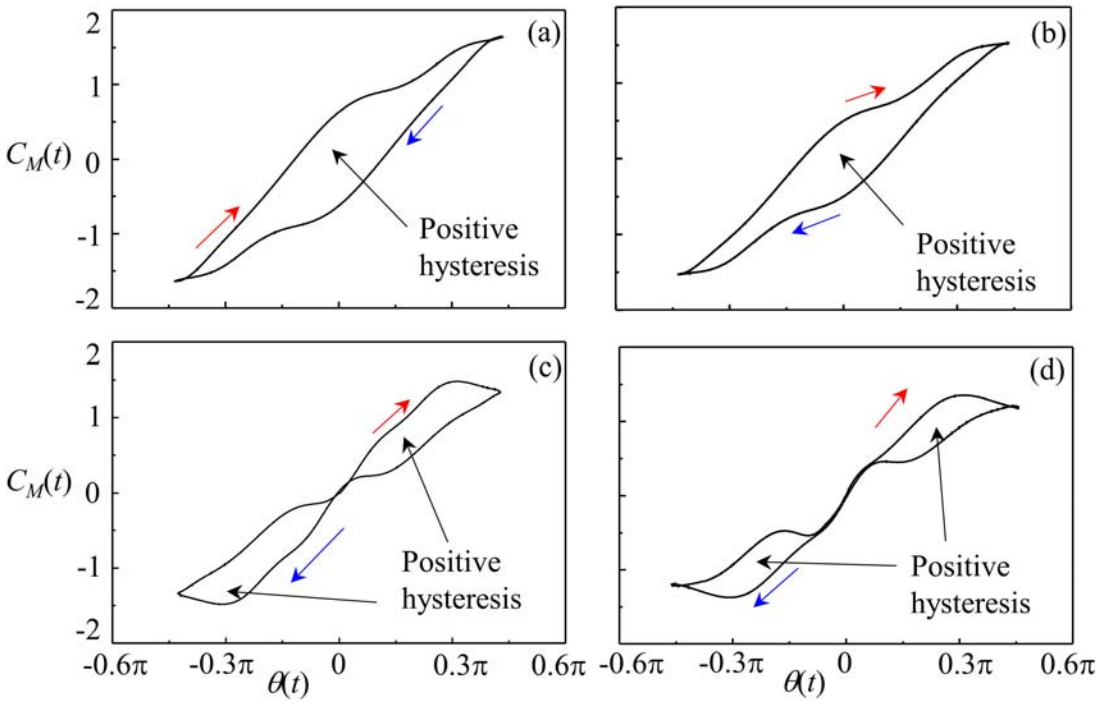

FIG. 9. Phase planes of $C_M(t)$ vs $\theta(t)$ at $\zeta = 0.130$ for (a) $Ur = 37$, (b) $Ur = 39$, (c) $Ur = 42$, and (d) $Ur = 45$.

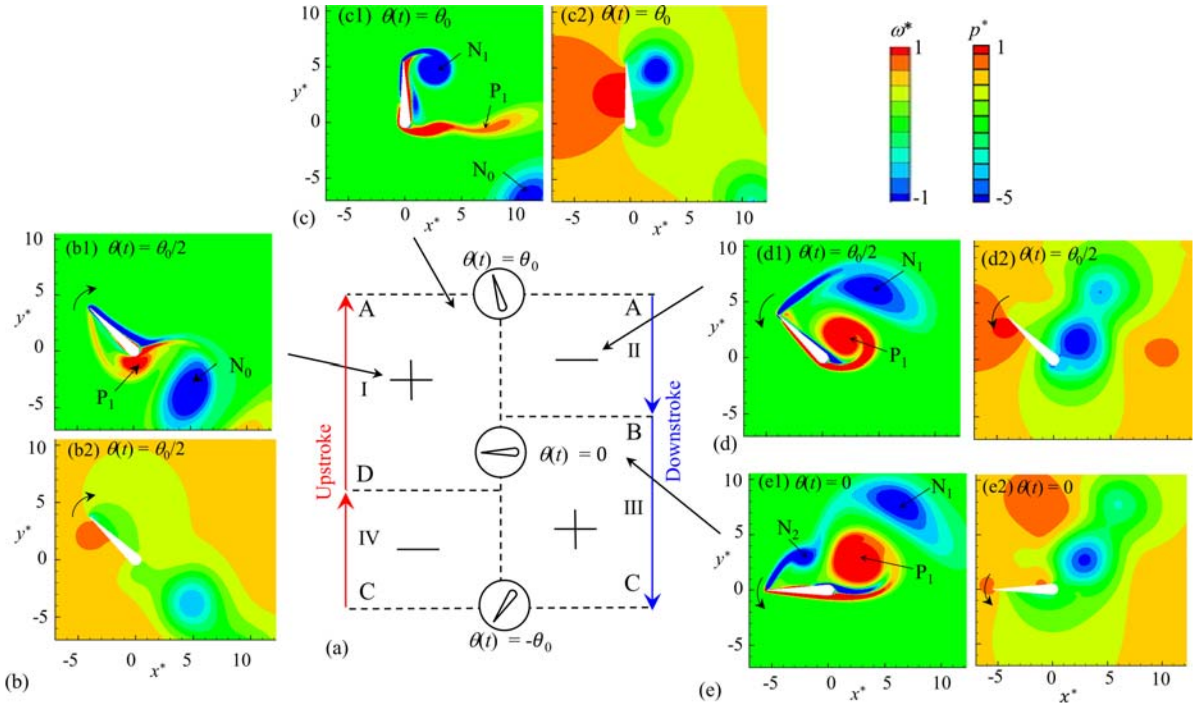

FIG. 10. (a) Power exchange diagram. [(b)–(e)] Corresponding vorticity (ω^*) structures [(b1), (c1), (d1), and (e1)] and pressure (p^*) distributions [(b2), (c2), (d2), and (e2)]. $Ur = 37$ and $\zeta = 0.130$.

remains positive against negative $\dot{\theta}$ [Fig. 8(a)]. Negative power thus comes into being, the foil releasing energy to the fluid. When the foil travels from $\theta = \theta_0/2$ to $\theta = 0$ [Fig. 10(e)], the signs of pressure swap between the upper and lower surfaces, generating negative C_M against negative $\dot{\theta}$. The power is therefore positive at $\theta = 0$. Both base and top vortices (N_1, N_2, and P_1) appear on the upper side of the foil while the lower boundary layer remains attached on the lower surface. Interestingly, the vortices strongly change and grow from $\theta = \theta_0$ to $\theta = \theta_0/2$ [Figs. 10(c) and 10(d)] where they receive energy from the foil. Comparing Figs. 10(b) and 10(d) corresponding to the positive and negative power, respectively (both at $\theta = \theta_0/2$), it is understood that strong vortices are generated from the foil at $\theta = \theta_0/2$ [Fig. 10(d)] where negative power is produced. On the other hand, no strong vortices appear at the state of positive power [Fig. 10(b)]. It can thus be concluded that the vortices strongly roll and receive energy from the foil in the negative power region. On the other hand, in the positive power region, the foil receives energy from the flow, and vortices are weak. In other words, vortices grow less and more when the foil receives energy and transfers energy, respectively. The above information as to the relationship between vortex growth and power is very fancy and can be used to enhance the power by suppressing or weakening the vortex formation in the return stroke. In a free vibration test of two elastically mounted tandem cylinders, Qin *et al.* found two types of vortices in the wake.[47] One type of vortices does positive work on the cylinder and vanishes rather rapidly in the wake. On the other hand, the other type is well-structured and stronger, connected to a negative work done on the cylinder. Moreover, given that the foil rotates around the center of the semicircular trailing edge, the pressure change around the trailing edge may have a minimum contribution to the total moment. As such, the trailing edge flow separation may have a much smaller contribution to the energy harvesting compared to the leading-edge flow separation.

4. *Effects Ur and ζ on flow structure*

Figure 11 presents the vorticity structures for $Ur = 37$ and 45 when $\zeta = 0.055$. As seen in Figs. 11(a) and 11(b), when Ur is increased from 37 to 45, the vorticity structure changes in size, spatial arrangement, and ω^* magnitudes. At $\theta = \theta_0/2$ [forward stroke, Fig. 11(a1)], the flow at $Ur = 37$ displays a positive vortex P_{a1} and a negative vortex N_{a0}, the former rolling on the trailing edge of the foil. Although generated from the upper side of the foil in the previous cycle, vortex N_{a0} lies below the symmetric line ($y^* = 0$). On the other hand, for $Ur = 45$ [Fig. 11(b1)], negative vortex N_{b0} and positive vortex P_{b1} both are enfeebled, yet not well-structured, compared to the counterparts in the case of $Ur = 37$. When the foil arrives at its maximum displacement [$\theta = \theta_0$, Figs. 11(a2) and 11(b2)], the wake structures for $Ur = 37$ and 45 are qualitatively similar to each other. The negative vortex is more matured and away from the foil for $Ur = 45$ than for $Ur = 37$. The negative vortices (N_{a1} and N_{b1}) generated at $\theta = \theta_0$ enlarge in size in the return stroke [$\theta = \theta_0/2$, Figs. 11(a3) and 11(b3)] as do positive vortices (P_{a1} and P_{b1}). In particular, the distance ξ between the dipole increases from $Ur = 37$ to 45, i.e., $\xi_b > \xi_a$ [Figs. 11(a3) and 11(b3)]. The convective velocity of N_{b1} is higher than that of N_{a1}, which can be understood from the comparison of the streamwise movements of N_{b1} and N_{a1} between $\theta = \theta_0$ and $\theta = \theta_0/2$ (return stroke). At $\theta = 0$ [Figs. 11(a4) and 11(b4)], the negative vortex (N_{a1} and N_{b1}) pinches off while another new vortex (N_{a2} and N_{b2}) is born. Vortex P_{a1} for $Ur = 37$ yet receives vorticities from the shear layer while the corresponding vortex P_{b1} for $Ur = 45$ is about to pinch off. The observations suggest that an increase in Ur may cause a change in the phase lag between θ and lift force C_L as well as between θ and C_M.

The ζ effect on vorticity structures can be studied by comparing the vorticity results for $Ur = 37$ between $\zeta = 0.055$ [Fig. 11(a)] and $\zeta = 0.130$ [Figs. 10(b1), 10(c1), 10(d1), and 10(e1)]. Vorticity structures at both $\zeta = 0.055$ and 0.130 are qualitatively similar. There are, however, differences in vorticity concentrations and vortex phases between $\xi = 0.055$ and 0.130. For example, vortex P_1 at $\theta = \theta_0$ for $\zeta = 0.130$ is slightly bigger than vortex P_{a1} for $\zeta = 0.055$ [Figs. 10(b1) and 11(a1)]. Their (P_1 and P_{a1}) shapes appear different at $\theta = \theta_0$ [Figs. 10(c1) and 11(a2)] where P_1 starts to roll up while P_{a1} appears like a shear layer. At $\theta = 0$, vortices N_2 and N_1 for $\zeta = 0.130$ leads the corresponding vortices N_{a2} and N_{a1} for $\zeta = 0.055$, N_2 having more vorticity

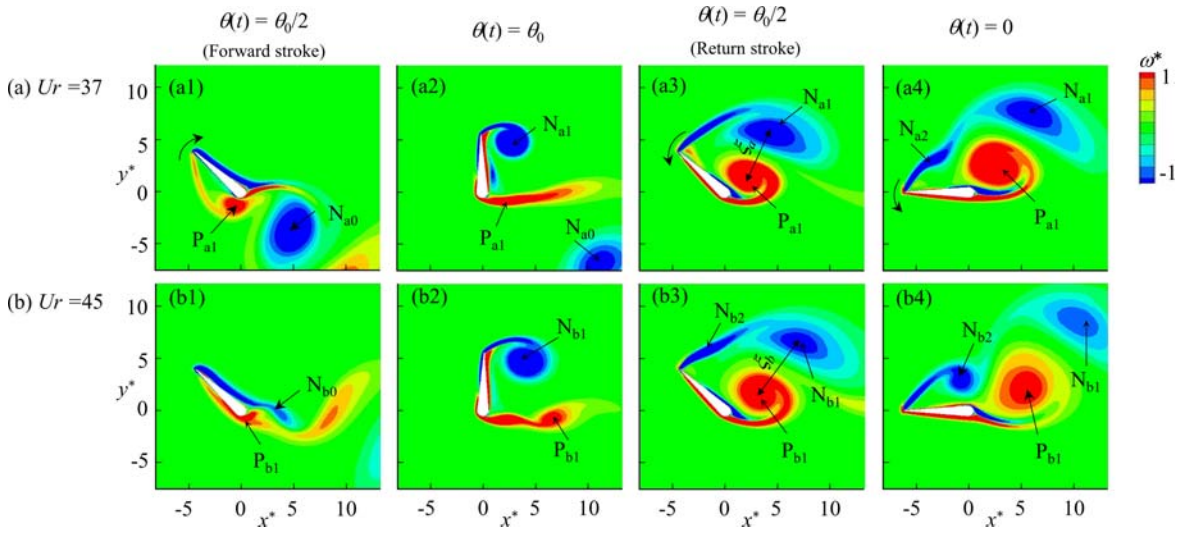

FIG. 11. Comparison of spanwise vorticity ω^* structures between (a) $Ur = 37$ and (b) $Ur = 45$ at $\zeta = 0.055$.

concentration than N$_{a2}$ [Figs. 11(a4) and 10(e1)]. That is, a change in ζ causes a change in the vortex phase, hence the phase lag between θ and lift force C_L and/or between θ and C_M.

5. *Drag and lift forces*

Time-dependent drag coefficient C_d ($= F_x/0.5\rho {U_\infty}^2 c$) and lift coefficient C_L ($= F_y/0.5\rho {U_\infty}^2 c$) for $Ur = 37$ and 45 with $\zeta = 0.055$ are presented in Fig. 12, where F_x and F_y are the drag and lift forces acting on the foil, respectively. To assimilate C_d and C_L evolutions during the foil's pitching, we first define the foil's locomotion in phase ϕ space [Fig. 12(a)]. The $\phi = 0$–2π labels one pitching period with $\phi = 0$ and π pinpointing $\theta = 0$ while $\phi = \pi/2$ and $3\pi/2$ pinpointing $\theta = \theta_0$ and $-\theta_0$, respectively [Fig. 12(a)]. As shown in Fig. 12(b), C_d increasing in the forward stroke (FS) reaches its maximum in the early return stroke. The peak is, however, slightly delayed for $Ur = 45$ compared to that for $Ur = 37$. One question may arise why the maximum C_d occurs in the early return stroke. Note that when the foil returns from the extreme to the mean position, the foil tip moves in the direction opposite to the freestream flow. The effective flow velocity (flow velocity with respect to foil) in the early return stroke is thus high as is the effective bluff width (projection of c normal to the freestream flow). This makes the occurrence of maximum C_d in the early return stroke. It worth mentioning that a forced pitching foil undergoes maximum thrust when it tends to return from its extreme position.[45] The C_d, on the other hand, is minimum just before the foil reaching its mean ($\phi = \pi$) position. As such, C_d has two periods in one pitching period of the foil, the second period being the time translation symmetry of the first period. The maximum C_d declines with Ur increasing from 37 to 45.

Unlike C_d, the C_L has one period in one pitching period, its magnitude being maximum after the foil crossing the mean position [Fig. 12(c)]. Its value is close to zero when the foil is close to its extreme position ($\phi = \pi/2$). It would be interesting to see how the total force coefficient $C_t = \sqrt{C_d^2 + C_L^2}$ and phase angle $\alpha = \tan^{-1}(C_L/C_d)$ vary in one pitching period. As seen in Figs. 13(a) and 12(b), the C_t trend is similar to C_d as C_t is mainly determined by C_d, with the amplitude of C_d variation being about two times higher than that of C_L (Fig. 12). The C_t yet peaks in the early return stroke and dips to a minimum before reaching the mean position. Although C_d and C_L are found to be small or close to zero for certain ϕ values (Fig. 12), C_t is not close to zero any more, but significantly high (Fig. 13), as the occurrence of small C_d and C_L is not at the same ϕ value (Fig. 12). Figure 13(b) shows that α largely follows C_L curve. When the foil is close to the mean position (e.g., $\phi < \pi/8$), the magnitude of α is as large as $\alpha > 0.75\pi/2$, indicating that C_t largely acts in the lift direction. On the other hand, when the foil is close to its extreme position (i.e., $3\pi/8 < \phi < 5\pi/8$), α is close to zero, signifying that C_t is largely directed in the drag direction.

IV. CONCLUSIONS

Energy harvesting from a passively oscillating inverted foil is numerically studied at a thickness-based Reynolds number $Re_D = 150$. In the case of the undamped system ($\zeta = 0$), the foil is not self-excited until $Ur = 27$ but is excited for $Ur > 27$. The oscillation amplitude θ_0 grows from 0 to $\approx 0.54\pi$ for $27 < Ur < 34$, remaining more or less constant of $\theta_0 \approx 0.54\pi$ for $Ur \geq 34$. The foil requires a longer time in the return stroke than in the forward strokes. The positive power hysteresis appears at $|\theta| < \theta_0/2$, while the negative power hysteresis persists at $|\theta| > \theta_0/2$, the net power being zero.

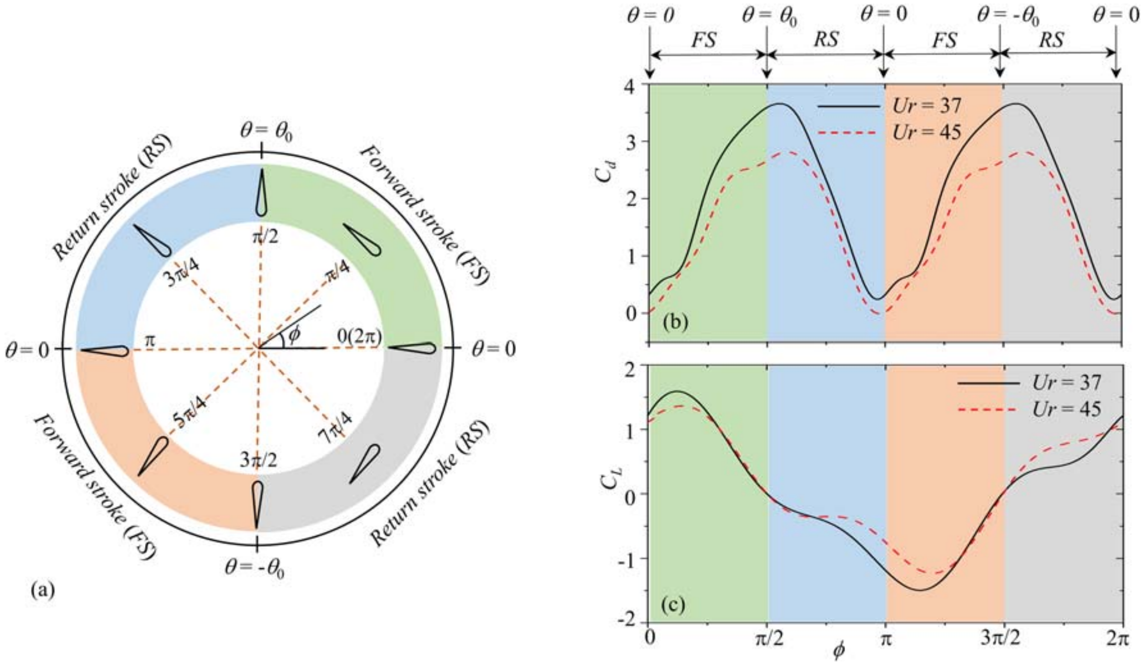

FIG. 12. (a) Definition of foil's locomotion in phase ϕ space. Instantaneous (b) drag coefficient C_d and (c) lift coefficient C_l acting on the foil at $\zeta = 0.055$.

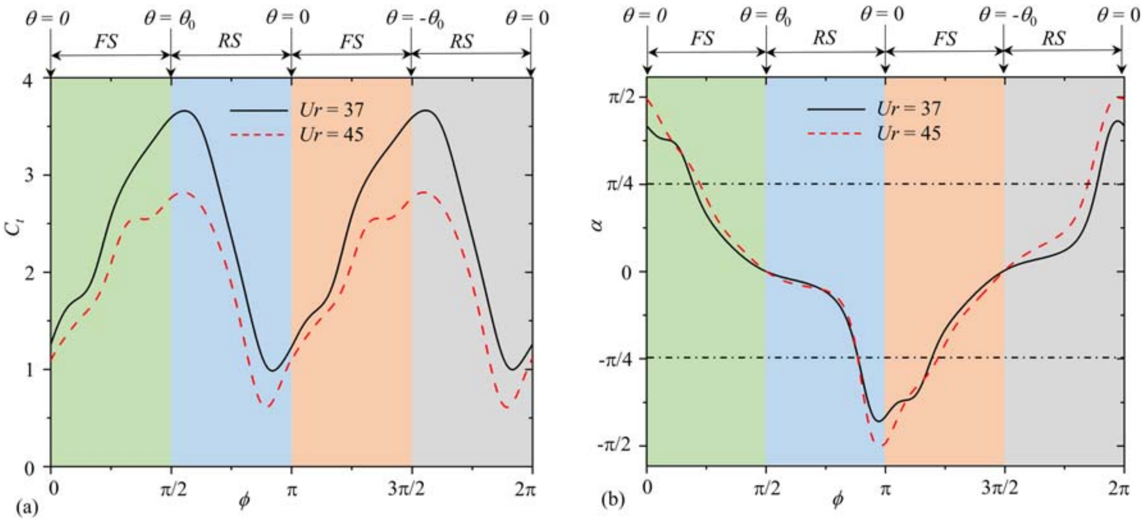

FIG. 13. Variations in (a) C_t and (b) α with ϕ at $\zeta = 0.055$.

The power exchange between the foil and fluid is studied for $Ur = 37$ with $\zeta = 0.035$–0.295. For $\zeta < 0.130$, both positive and negative power hysteresis appear in the phase planes of $C_M(t)$ vs $\theta(t)$, similar to that for the undamped case. When ζ increases from 0.035 to 0.295, the positive hysteresis region grows, reaching a maximum at $\zeta = 0.130$ before declining, while the negative hysteresis region shrinks and vanishes at $\zeta = 0.130$. The maximum power and efficiency thus occur at $\zeta = 0.130$ with distinguished foil responses at $\zeta < 0.130$ and $\zeta > 0.130$. The foil velocity is larger in the forward stroke than in the return stroke for $\zeta < 0.130$ while the opposite is the case for $\zeta > 0.130$. Both oscillation amplitude and frequency reduce when ζ is increased from 0.035 to 0.295. The reduction is however less in $\zeta = 0.035$–0.130 than in $\zeta = 0.130$–0.295. The maximum efficiency corresponds to the reduced frequency $f^* = 0.151$ that is usually adopted by the cruising aquatic animals.

The link between vortex formation and energy extraction is imparted. The vortices radically change and grow when the foil releases energy to the flow, i.e., the foil oscillation enhances the growth of the vortices. On the other hand, when the foil extracts energy from the flow, vortices grow less and receive less energy from the flow. This work provides important findings for a better understanding of the power exchange between the fluid and the free oscillating foil. The findings may be useful to design energy harvesters in rivers, nearshore waters, or water canals. In addition, more work is required on multiple inverted foils to enhance efficiency and to generalize the practical applicability of energy harvesters.

ACKNOWLEDGMENTS

The authors would like to acknowledge the support received from the Deanship of Scientific Research (DSR), King Fahd University of Petroleum & Minerals (KFUPM) under University Funded Grant No. DF191002. The authors also greatly acknowledge the contribution of Mr. Wu Zhen to simulation.

DATA AVAILABILITY

The data that support the findings of this study are available within the article.

REFERENCES

[1] Z. M. Salameh and L. Safari, "Optimum windmill-site matching," IEEE Trans. Energy Convers. **7**, 669–676 (1992).
[2] S. Oerlemans, P. Sijtsma, and B. Méndez Lopez, "Location and quantification of noise sources on a wind turbine," J. Sound Vib. **299**, 869–883 (2007).
[3] Z. Chen, M. M. Alam, B. Qin, and Y. Zhou, "Energy harvesting from and vibration response of different diameter cylinders," Appl. Energy **278**, 115737 (2020).
[4] B. Seyed-Aghazadeh, H. Samandari, and S. Dulac, "Flow-induced vibration of inherently nonlinear structures with applications in energy harvesting," Phys. Fluids **32**, 071701 (2020).
[5] A. K. Soti and A. De, "Vortex-induced vibrations of a confined circular cylinder for efficient flow power extraction," Phys. Fluids **32**, 033603 (2020).
[6] P. Han, P. Hemon, G. Pan, and E. de Langre, "Nonlinear modeling of combined galloping and vortex-induced vibration of square sections under flow," Nonlinear Dyn. **103**, 3113–3125 (2021).
[7] C. Ji, Y. Cui, D. Xu, X. Yang, and N. Srinil, "Vortex-induced vibrations of dual-step cylinders with different diameter ratios in laminar flows," Phys. Fluids **31**, 073602 (2019).
[8] J. Young, J. C. S. Lai, and M. F. Platzer, "A review of progress and challenges in flapping foil power generation," Prog. Aerosp. Sci. **67**, 2–28 (2014).
[9] Q. Schiermeier, J. Tollefson, T. Scully, A. Witze, and O. Morton, "Electricity without carbon," Nature **454**, 816–823 (2008).
[10] T. Kinsey and G. Dumas, "Parametric study of an oscillating airfoil in a power-extraction regime," AIAA J. **46**, 1318–1330 (2008).
[11] T. Kinsey, G. Dumas, G. Lalande, J. Ruel, A. Mehut, P. Viarouge, J. Lemay, and Y. Jean, "Prototype testing of a hydro kinetic turbine based on oscillating foils," Renewable Energy **36**, 1710–1718 (2011).
[12] Q. Zhu, "Optimal frequency for flow energy harvesting of a flapping foil," J. Fluid Mech. **675**, 495–517 (2011).
[13] G. K. Taylor, R. L. Nudds, and A. Thomas, "Flying and swimming animals cruise at a Strouhal number tuned for high power efficiency," Nature **425**, 707–711 (2003).

[14] C. Eloy, “Optimal Strouhal number for swimming animals,” J. Fluids Struct. **30**, 205–218 (2012).

[15] M. Gazzola, M. Argentina, and L. Mahadevan, “Scaling macroscopic aquatic locomotion,” Nat. Phys. **10**, 758–761 (2014).

[16] S. Barbarelli, G. Florio, M. Amelio, and N. M. Scornaienchi, “Preliminary performance assessment of a novel on-shore system recovering energy from tidal currents,” Appl. Energy **224**, 717–730 (2018).

[17] E. Shimizu, K. Isogai, and S. Obayashi, “Multi objective design study of a flapping wing power generator,” J Fluids Eng. **130**, 021104 (2008).

[18] Q. Zhu, M. Haase, and C. H. Wu, “Modeling the capacity of a novel flow-energy harvester,” Appl. Math. Model. **33**, 2207–2217 (2009).

[19] Q. Zhu and Z. L. Peng, “Mode coupling and flow energy harvesting by a flapping foil,” Phys. Fluids **21**, 033601 (2009).

[20] H. Abiru and A. Yoshitake, “Study on a flapping wing hydroelectric power generation system,” J. Environ. Eng. **6**, 178–186 (2011).

[21] L. B. Teng, J. Deng, D. Y. Pan, and X. M. Shao, “Effects of non-sinusoidal pitching motion on energy extraction performance of a semi-active flapping foil,” Renewable Energy **85**, 810–818 (2016).

[22] Z. Liu, H. L. Qu, and H. D. Shi, “Energy-harvesting performance of a coupled-pitching foil under the semi-passive mode,” Appl. Energy **267**, 114889 (2020).

[23] J. Young, M. A. Ashraf, J. C. S. Lai, and M. F. Platzer, “Numerical simulation of fully passive flapping foil power generation,” AIAA J. **51**, 2727–2739 (2013).

[24] W. Li, W. Wang, Y. Yan, and F. B. Tian, “Effects of pitching motion profile on energy harvesting performance of a semi-active flapping foil using immersed boundary method,” Ocean Eng. **163**, 94–106 (2018).

[25] Z. L. Peng and Q. Zhu, “Energy harvesting through flow-induced oscillations of a foil,” Phys. Fluids **21**, 123602 (2009).

[26] K. Onoue, A. Song, B. Strom, and K. S. Breuer, “Large amplitude flow-induced oscillations and energy harvesting using a cyber-physical pitching plate,” J. Fluids Struct. **55**, 262–275 (2015).

[27] Z. Wang, L. Du, J. S. Zhao, and X. F. Sun, “Structural response and energy extraction of a fully passive flapping foil,” J. Fluids Struct. **72**, 96–113 (2017).

[28] D. Kumar, K. Poddar, and S. Kumar, “Flow-induced oscillation of a rigid rectangular plate hinged at its leading edge,” Phys. Fluids **30**, 063601 (2018).

[29] Z. Liu, H. L. Qu, and H. D. Shi, “Numerical study on hydrodynamic performance of a fully passive flow-driven pitching foil,” Ocean Eng. **177**, 70–84 (2019).

[30] S. P. Sane, “The aerodynamics of insect flight,” J. Exp. Biol. **206**, 4191–4208 (2003).

[31] A. J. Bergou, S. Xu, and Z. J. Wang, “Passive wing pitch reversal in insect flight,” J. Fluid Mech. **591**, 321–337 (2007).

[32] J. P. Whitney and R. J. Wood, “Aeromechanics of passive rotation in flapping flight,” J. Fluid Mech. **660**, 197–220 (2010).

[33] D. Kim, J. Cossé, C. Huertas-Cerdeira, and M. Gharib, “Flapping dynamics of an inverted flag,” J. Fluid Mech. **736**, R1 (2013).

[34] P. S. Gurugubelli and R. Jaiman, “Self-induced flapping dynamics of a flexible inverted foil in a uniform flow,” J. Fluid Mech. **781**, 657–694 (2015).

[35] A. Goza, T. Colonius, and J. E. Sader, “Global modes and nonlinear analysis of inverted-flag flapping,” J. Fluid Mech. **857**, 312–344 (2018).

[36] P. S. Gurugubelli and R. Jaiman, “Large amplitude flapping of an inverted elastic foil in uniform flow with spanwise periodicity,” J. Fluids Struct. **90**, 139–163 (2019).

[37] S. Michelin and O. Doaré, “Energy harvesting efficiency of piezoelectric flags in axial flows,” J. Fluid Mech. **714**, 489–504 (2013).

[38] L. Tang, M. P. Paidoussis, and J. Jiang, “Cantilevered flexible plates in axial flow: Energy transfer and the concept of flutter-mill,” J. Sound Vib. **326**, 263–276 (2009).

[39] K. Shoele and R. Mittal, “Energy harvesting by flow-induced flutter in a simple model of an inverted piezoelectric flag,” J. Fluid Mech. **790**, 582–606 (2016).

[40] F. M. Bos, D. Lentink, B. W. van Oudheusden, and H. Bijl, “Influence of wing kinematics on aerodynamic performance in hovering insect flight,” J. Fluid Mech. **594**, 341–368 (2008).

[41] S. Wang, D. B. Ingham, L. Ma, M. Pourkashanian, and Z. Tao, “Numerical investigations on dynamic stall of low Reynolds number flow around oscillating airfoils,” Comput. Fluids **39**, 1529–1541 (2010).

[42] I. Robertson, L. Li, S. J. Sherwin, and P. W. Bearman, “A numerical study of rotational and transverse galloping rectangular bodies,” J. Fluids Struct. **17**, 681–699 (2003).

[43] A. Andersen, T. Bohr, T. Schnipper, and J. H. Walther, “Wake structure and thrust generation of a flapping foil in two-dimensional flow,” J. Fluid Mech. **812**, R4 (2017).

[44] L. M. Chao, G. Pan, D. Zhang, and G. X. Yan, “Numerical investigations on the force generation and wake structures of a nonsinusoidal pitching foil,” J. Fluids Struct. **85**, 27–39 (2019).

[45] M. M. Alam and Z. Muhammad, “Dynamics of flow around a pitching hydrofoil,” J. Fluids Struct. **99**, 103151 (2020).

[46] L. M. Chao, M. M. Alam, and C. Ji, “Drag-thrust transition and wake structures of a pitching foil undergoing asymmetric oscillation,” J. Fluids Struct. **103**, 103289 (2021).

[47] B. Qin, M. M. Alam, and Y. Zhou, “Free vibrations of two tandem elastically mounted cylinders in cross-flow,” J. Fluid Mech. **861**, 349–381 (2019).